Letter

Omnidirectional domain wall modes protected by fragile topological states

Pegah Azizi,[1] Siddhartha Sarkar,[2] Kai Sun,[2] and Stefano Gonella[1,*]
[1]*Department of Civil, Environmental, and Geo- Engineering, University of Minnesota, Minneapolis, Minnesota 55455, USA*
[2]*Department of Physics, University of Michigan, Ann Arbor, Michigan 48109, USA*

(Received 7 December 2023; revised 8 July 2024; accepted 6 August 2024; published 20 August 2024)

So-called fragile topological states of matter challenge our conventional notion of topology by lacking the robustness typically associated with topological protection, thereby displaying elusive manifestations that are difficult to harness for wave control. In this Letter, we leverage the recent discovery of fragile topological states in special classes of structural kagome lattices to document the availability of domain wall elastic wave modes that are directly traceable to fragile topology and, yet, exhibit remarkably strong signatures that support omnidirectionality. We design twisted kagome bidomains comprising two topologically distinct sublattices—one trivial and the other fragile topological—sharing a common band gap and meeting at a domain wall. The two phases are achieved via carefully engineered surface cut patterns that modify the band landscape of the underlying lattices in complementary fashions, leading to dichotomous irreps landscapes. Under these circumstances, a domain wall-bound mode emerges within the shared band gap and displays remarkable stability against domain wall orientation and introduced defects. We corroborate these findings via $\mathbf{k}\cdot\mathbf{p}$ Hamiltonian and Jackiw-Rebbi analysis and validate them experimentally through laser vibrometry tests on a prototype endowed with water-jet-induced perforation patterns.

DOI: 10.1103/PhysRevB.110.L060102

Maxwell lattices [1,2] have received substantial attention in recent years due to an array of unique mechanical properties, including the ability to localize deformation at floppy edges [3–7] and focus stress at domain walls (DWs), thus eliciting protection against fracture and buckling [8,9], and tunable multistability [10]. A popular subclass of Maxwell systems, kagome lattices have been extensively studied, especially in the realm of ideal configurations characterized by perfect hinges, for the peculiar properties rooted in their topology and symmetries [11–17]. Many topological properties of Maxwell lattices have been shown to be preserved, albeit diluted, in transitioning from *ideal* to *structural* lattices that can be physically fabricated, where the bonds can carry flexural deformation and the hinges are replaced by internal clamps or by ligaments featuring finite stiffness against rotations [18–23].

Recent studies have put forth the notion of fragile topology [24–35]. Fragile bands qualify as topological in that they do not admit a symmetric, exponentially localized Wannier representation that preserves all the symmetries of the system. However, unlike stable topology, their obstruction to the atomic limit can be eliminated by coupling with fully topologically trivial bands. Additionally, these states generally lack a well-defined conventional bulk-edge correspondence [36–40]. A recent investigation by Azizi *et al.* explored fragile topology in the context of twisted kagome lattices in the so-called self-dual configuration [18]. The term *self-dual*, introduced by Fruchart *et al.* within their treatment of mechanical duality of twisted kagome lattices [41], refers to the critical point in configuration space that separates families of dual pairs, which feature identical phononic properties [12,41,42]. The authors of [18] proved theoretically and demonstrated experimentally the existence of fragile topological states in self-dual kagome lattices in the *structural* configuration featuring ligamentlike hinges at the lattice sites. However, while they identified a number of localized modes, for none of them could a direct connection to fragile topology or claims of topological protection be made.

This Letter aims at filling this conceptual gap by deliberately searching for localized modes that are unequivocally linked to, and protected by, the fragile topology. We seek such modes along the DWs of bidomain lattices obtained by adjoining two structural self-dual twisted kagome (SSTK) sublattices with different topological character—one trivial and the other fragile topological—making sure that the two phases are designed to be spectrally compatible. The proposed approach draws partial inspiration from the behavior of mechanical analogs of the quantum valley-Hall effect (QVHE) [43–47], where domain-bound modes can be generated at the DW of two subdomains characterized by opposite valley topologies bounding a shared band gap (BG) [48]. A byproduct objective of our study is to address a limitation of QVHE analogs, which support DW modes along various orientations [49,50] except for specific forbidden directions. In contrast, here we put forth a strategy to achieve truly omnidirectional DW mode localization capability along any arbitrary direction.

We begin our analysis resuming the SSTK configuration presented in [18], which features fragile topological bands. Recall that the configuration consists of a self-dual kagome in which the triangles are solid patches, taken to be thin to realize plane-stress conditions, connected by finite-thickness

*Contact author: sgonella@umn.edu

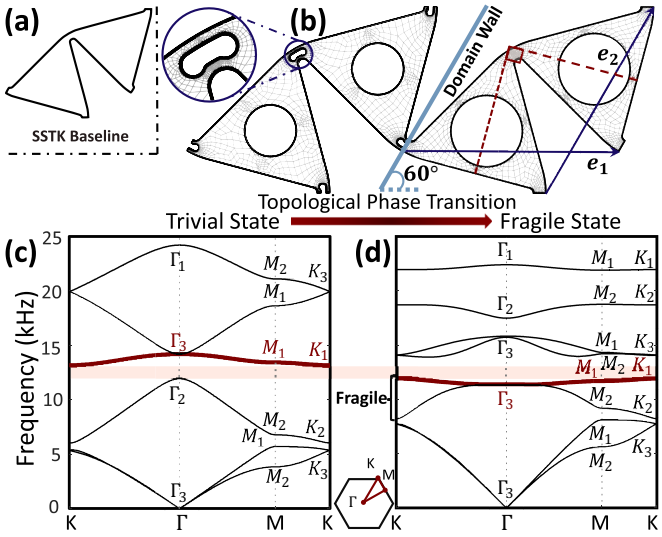

FIG. 1. (a) Unit cell of SSTK baseline configuration. (b) Bidomain lattice with DW obtained stitching a trivial and a fragile topological SSTK phase. Inset: Zoomed-in detail of the bean-shaped hole at the hinge of the trivial phase. Both configurations feature large holes to modulate inertia and control frequency spectra. (c),(d) Band diagrams of the trivial and fragile topological states, respectively. The thick maroon branch denotes the band undergoing inversion, leading to the closing and reopening of the shared BG (shaded in pink) marking the topological phase transition. The irreps at HSPs of the BZ confirm the topological nature of the third and fourth bands in (d).

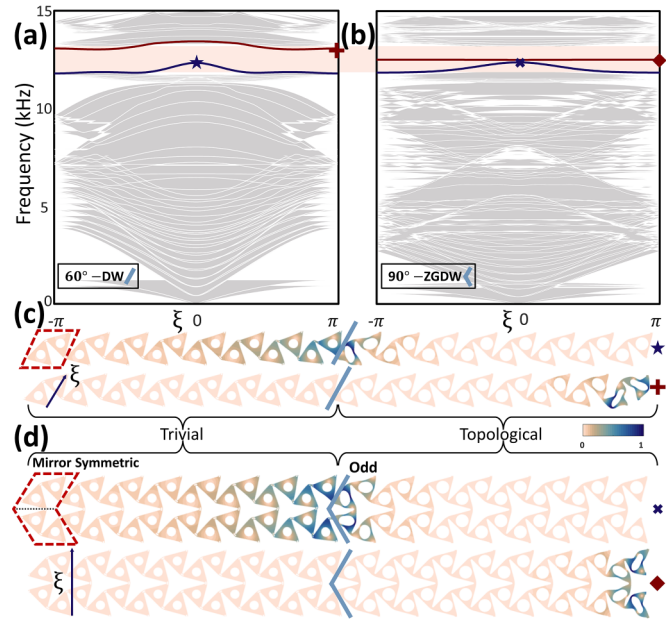

FIG. 2. (a),(b) Band diagrams for two differently oriented 16-cell SSTK supercells (with unit cells highlighted) forming (a) $60^\circ - \mathrm{DW}$ and (b) $90^\circ - \mathrm{ZGDW}$, with branches for the DW mode and edge modes highlighted in blue and maroon, respectively. (c),(d) Wave functions (mode shapes) of localized DW and edge states for the $60^\circ - \mathrm{DW}$ and $90^\circ - \mathrm{ZGDW}$, sampled at $\xi = 0$ and $\xi = \pi$. The left and right sides consist of trivial and topological states, respectively.

ligaments. Our objective is to extract from this baseline geometry two topologically distinct derivative configurations—one trivial and the other topological—that are simultaneously geometrically and spectrally compatible. Geometric compatibility requires that the lattices can be seamlessly stitched to form a DW, which implies that they shall share the same unit cell primitive lattice vectors and C_{3v} point group symmetry. Moreover, in anticipation of the construction of an experimental prototype, we seek configurations that are practically feasible under the constraints of the available fabrication methods. Specifically, we want the lattices to be monomaterial, as to be agilely obtainable via subtractive manufacturing (e.g., machining or water-jet cutting) from a slab of homogeneous, low-damping material with uniform and predictable properties, e.g., a metal. We also require that the two lattices deviate from each other only in terms of different patterns of cuts introduced *a posteriori* as a perturbation of the shared baseline SSTK geometry. This ensures that the thickness of the hinges, which is a critical parameter, is preserved across the DW. Finally, we want the two configurations to be spectrally compatible, i.e., to feature a shared full BG in the midfrequency region of the spectrum.

The first step of the design process consists of modifying the topological SSTK baseline configuration [Fig. 1(a)] to induce a transition to a trivial configuration, marked by the closing and reopening of the midfrequency BG. An avenue towards this phase transition is by softening the hinge ligament of the unit cell, as explored in [18]. In light of the above-stated monomaterial constraint, here we seek an analogous softening effect purely by virtue of geometry. To this end, we introduce isolated cuts or clusters of cuts in the neighborhood of the hinges. After a few design iterations (see the Supplemental Material (SM), Sec. 1 [51]), we eventually land on the bean-shaped hole shown in the inset of Fig. 1(b). Notably, this addition results in the desired topological band inversion along with a substantial increase in BG width (SM, Sec. 1 [51]). To ensure spectral compatibility between the new trivial (with hole) and the original topological (holeless) configurations, we modulate their effective mass densities by endowing the unit cells of both configurations with additional holes and we fine tune their relative diameters until the two BGs have comparable width and align in the desired interval of the spectrum. The resulting geometries are shown in Fig. 1(b) in their stitched configuration, with the trivial phase featuring hinge holes and small density-correcting holes on the left of the DW, and the topological phase featuring intact hinges and large density-correcting holes on the right. The primitive lattice vectors are denoted as $\mathbf{e}_1$ and $\mathbf{e}_2$, with $\mathbf{e}_2$ aligned parallel to the DW, forming a 60° angle with the horizontal. The corresponding band diagrams are shown in Figs. 1(c) and 1(d), where we can observe the above-mentioned band inversion at the Γ point, whereby the fourth band (highlighted in maroon) appears above and below the shared BG, respectively. Additionally, we report irreducible representations (irreps) calculated at the high symmetry points (HSPs) of the Brillouin zone (BZ) following the procedure and notation given in the Bilbao crystallography server [52–56] based on the recently developed method of topological quantum

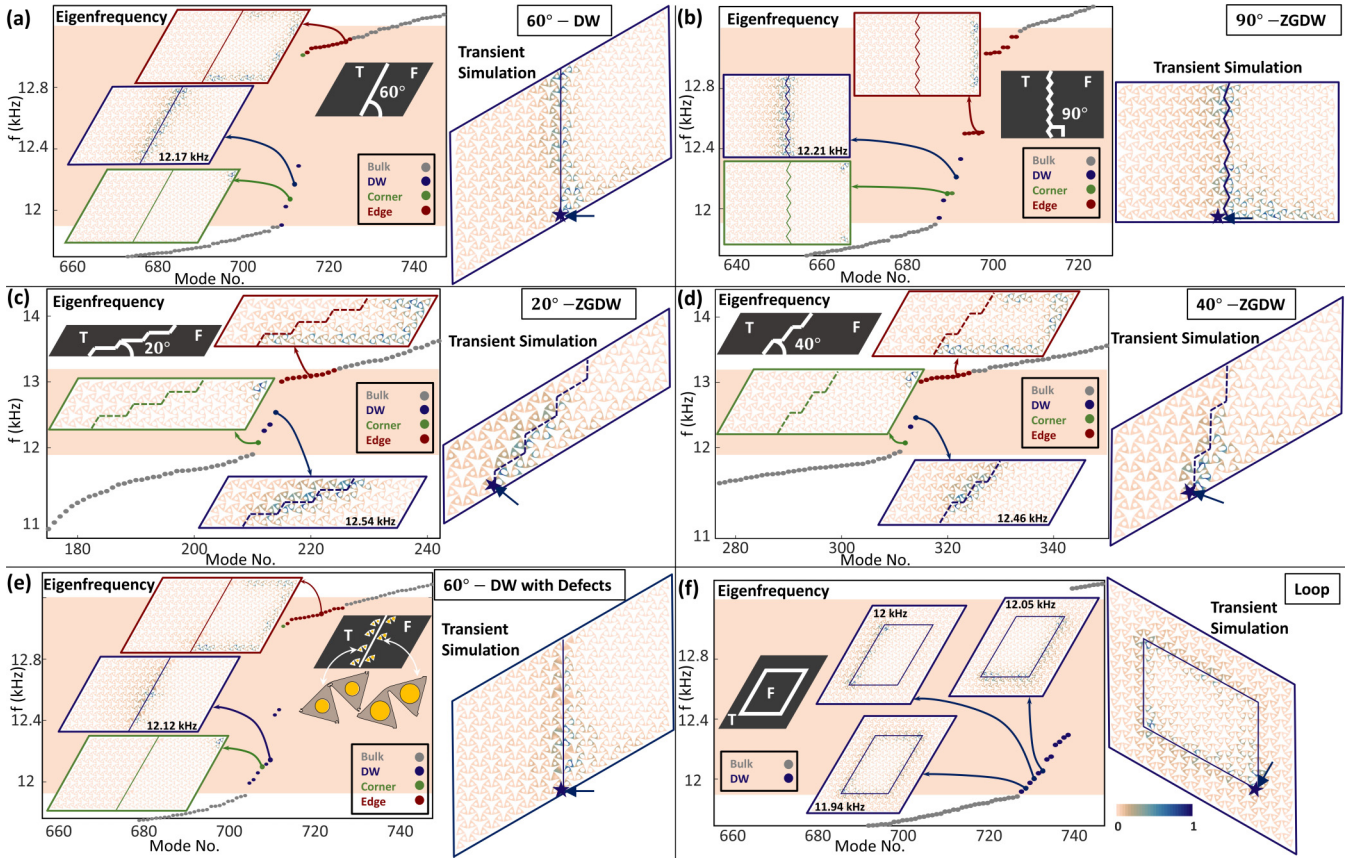

FIG. 3. (a)–(f) Dynamical response for six scenarios: (a) 60° − DW, (b) 90° − ZGDW, (c) 20° − ZGDW, (d) 40° − ZGDW, (e) 60° − DW with randomly located defects, and (f) internal loop. For each case, the left panel contains eigenfrequencies in the frequency interval of the shared BG, color-coded to distinguish bulk modes and different types of localized modes, including DW (with the corresponding frequency indicated), corner, and edge states, with three sample eigenfields shown in the insets. The right panel depicts snapshots of propagating wave fields (from full-scale transient simulations) induced by a narrow-band burst force excitation, polarized perpendicularly to the DW. In all cases, the wave is unequivocally localized along the DW.

chemistry, which classifies all topological states that are protected by spatial symmetries [57,58]. The irreps, which encapsulate the symmetry properties of the eigenmodes at the HSPs, provide a recipe to qualify the topology of isolated bands. The two-dimensional (2D) irrep Γ_3 and 1D irrep Γ_2 undergo band inversion from the case of Figs. 1(c) and 1(d), resulting in bands 3 and 4 for having now HSP irreps $\Gamma_3 - M_1 \oplus M_2 - K_1 \oplus K_2$ in Fig. 1(d), which implies these two bands are indeed fragile topological, protected by C_3 symmetry [18,29].

Having established a DW across which a topological phase transition occurs, we proceed to ask whether such DW can be the site of strongly localized modes and whether such modes enjoy any protection that is attributable to the fragile topology. Here, we consider two distinct versions of the bidomain lattice that can be realized by stitching trivial and fragile phases, one featuring a 60° − DW and the other 90° − zigzag DW (ZGDW). For each, we perform supercell analysis using a dedicated supercell. Specifically, the first supercell [Fig. 2(c)] is obtained from the tessellation of a single SSTK unit cell and intercepts the 60° − DW already discussed in Fig. 1. The other [Fig. 2(d)] consists of the tessellation of a mirror symmetric macrocell encompassing two unit cells, and results in a 90° − ZGDW globally perpendicular to the supercell itself and parallel to the direction of tessellation. The corresponding supercell band diagrams are shown in Figs. 2(a) and 2(b), respectively. In both configurations, we identify two relatively flat modes in the BG, which we recognize, from the mode shapes depicted in Figs. 2(c) and 2(d), as a DW mode and an edge mode, color coded in blue and maroon, respectively. The DW mode presents a few peculiarities. First, the availability of DW modes for both 60° − DW and 90° − ZGDW (as well as potentially along any other arbitrary direction, as demonstrated later in this Letter) represents an increase in versatility compared to QVHE, where DW modes are not achievable for angles of 90° (and, equivalently, 30° and 150°) (SM, Sec. 2 [51]). Here, the emergence of DW modes for any angle can be understood from the isotropic nature of the Γ point in a C_3 symmetric system. Moreover, most conventional topologically protected DW branches span the BG with quasiconstant finite slopes, denoting modes that propagate at finite velocities for any carrier frequency in the BG [44,45]. Here, in contrast, the relatively flat band results in the ability of the lattice to localize the signal in space with pronounced persistence over a frequency subinterval of the BG, while maintaining the overall gapped response. As for the edge modes, it is worth noting that they appear only in the fragile phase, where they display a high decay rate.

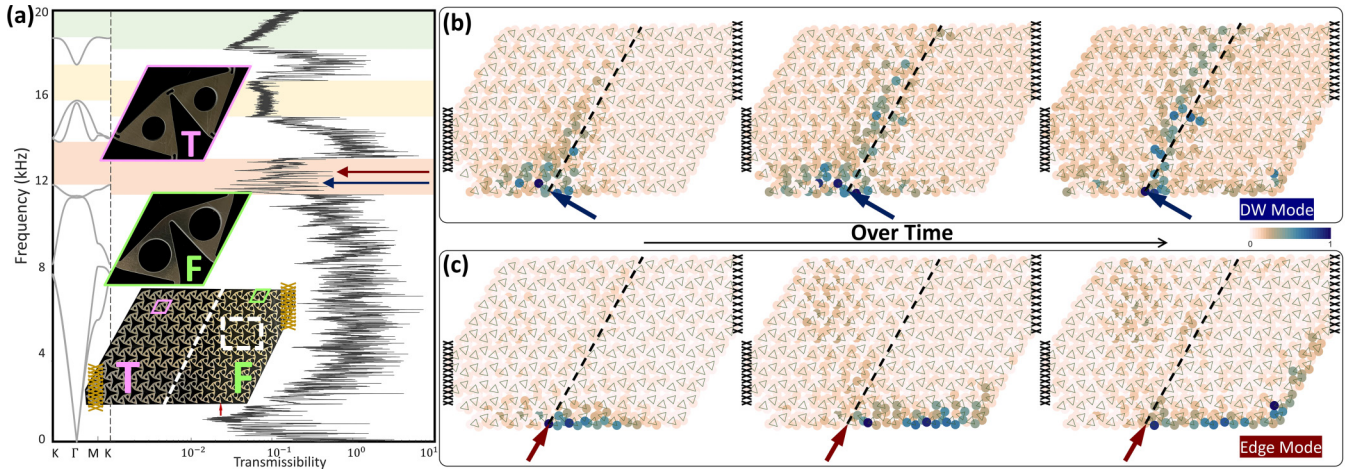

FIG. 4. (a) Laser vibrometry-acquired experimental transmissibility curve with highlighted attenuation regions reasonably matching the BG frequencies of the fragile phase spectrum plotted on the left. Insets provide details of the trivial (T) and fragile (F) unit cells of the water-jet-cut specimen. White dashed box denotes a region where the response is sampled. Blue and maroon arrows mark the excitation frequencies for the DW and edge modes activation, respectively. (b),(c) Snapshots of the measured wave fields induced by a 30-cycle burst with carrier frequencies corresponding to the DW and edge modes. Force polarization is indicated by the arrows. Color bar indicates velocity amplitude normalized by the highest value in each frame.

The emergence of the DW modes resulting from the topological phase transition marked by the band inversion between the Γ_2 and Γ_3 irreps can be analytically confirmed using Jackiw-Rebbi (JR) analysis [59]. In the SM, Sec. 2 [51], starting from a $\mathbf{k}\cdot\mathbf{p}$ Hamiltonian [60] near the Γ point of the BZ and considering only the bands with Γ_2 and Γ_3 irreps, we theoretically prove that DW modes must emerge between the trivial and fragile phases for any DW direction. Furthermore, we prove that the DW mode shapes obtained from the supercell analysis, shown in Figs. 2(c) and 2(d), are indeed caused by the topological phase transition between the trivial and fragile states by comparing them against those obtained from the JR analysis. It is worthwhile mentioning that since the $90^\circ-$ZGDW is mirror symmetric, a DW mode at this interface would have to be even or odd under the mirror reflection. It can be seen from Fig. 2(d) that the DW mode indeed has odd parity under the mirror—a feature captured by JR analysis. On the other hand, the $60^\circ-$DW breaks the mirror symmetry, and hence the DW mode does not have a definite parity, also predicted by the JR analysis.

Next, we evaluate eigenfrequencies and mode shapes for six finite bidomain configurations, depicted in Fig. 3, including $60^\circ-$DW [Fig. 3(a)], $90^\circ-$ZGDW [Fig. 3(b)], $20^\circ-$ZGDW [Fig. 3(c)], $40^\circ-$ZGDW [Fig. 3(d)], $60^\circ-$DW with defects [Fig. 3(e)], and loop [Fig. 3(f)]. In the configuration of Fig. 3(e), we randomly select seven unit cells close to the DW and we fill their central holes with inclusions, choosing a density ratio $\rho_{\text{inc}} = 0.8\rho_{\text{bulk}}$ to perturb the lattice order. In each of the cases in Figs. 3(a)–3(e), we report localized states in the BG frequency range: we recognize DW, corner, and edge modes, and we highlight a few randomly selected ones for each type by showing the corresponding eigenfunctions. Notably, in Figs. 3(a)–3(e), edge and corner modes localize exclusively along the edges of the fragile phase, consistent with the findings from supercell analysis. Finally, in the case of Fig. 3(f), we construct a closed DW loop to confine a parallelogram of fragile phase within a larger domain of the trivial phase and we perform a similar inference of the localized modes.

Subsequently, we provide additional evidence of DW emergence in the considered scenarios via full-scale transient simulations. Snapshots of computed propagating wave fields are displayed in the right part of each panel of Figs. 3(a)–3(f) under a point-force excitation, polarized perpendicular to the DW, prescribed at the bottom tip of the DW in the form of a 17-cycle narrow-band tone burst, with carrier frequency set at $\sim$12.2 kHz. Notably, in all cases, the wave fields exhibit pronounced localization along the DW, regardless of the DW orientation and the presence of defects.

We proceed to validate our theoretical findings through laser vibrometry experiments performed on a physical prototype (for detailed information regarding the fabrication, vibrometer specifications, and experimental setup, refer to the SM, Sec. 3 [51]). The specimen, along with zoomed-in details of the fragile and trivial unit cells, are displayed in the insets of Fig. 4(a). Our initial objective is to experimentally determine the BG frequencies. To accomplish this, we prescribe a broadband pseudorandom vertical excitation at a bottom edge point of the fragile phase (marked by a red arrow), we measure the in-plane vertical velocity at scan points inside a sampling region located away from the DW and the edges [dashed box in the inset of Fig. 4(a)], and we normalize the average velocity values with those recorded at the excitation point to construct a transmissibility curve versus frequency, as presented in Fig. 4(a) (see SM, Sec. 4 [51] for analogous curves obtained via full-scale steady-state simulation). Notably, the transmissibility reveals three distinct regions of attenuation, highlighted in lighter shades, which align well, within the expected deviations between model and experiments, with the BGs derived from Bloch analysis. The region shaded in pink marks the midfrequency BG of interest, within which we carry out two separate transient tests to empirically document the emergence of DW and edge modes. To this end, we excite

the bottom tip of the DW with bursts with carrier frequencies marked by the blue and maroon arrows in Fig. 4(a). We note that the frequency discrepancies between model and experiments prevent us from being able to precisely know the frequency of the localized modes *a priori*. Similarly, the transmissibility plot does not carry a sufficient spectral signature of them that can be leveraged. As a result, the identification of the carriers requires a heuristic approach in which we probe the frequency interval expected to be of interest based on analogy with simulations by conducting a series of tests with varying carriers until we detect the emergence of the desired modes. Eventually, we identify 12 and 12.5 kHz as the two frequencies of interest for the DW and edge modes, respectively. Specifically, if we apply a 30-cycle burst with a frequency of ∼12 kHz, polarized perpendicular to the DW direction, we generate a wave that propagates along the DW, three snapshots of which are depicted in Fig. 4(b). Similarly, Fig. 4(c) presents three snapshots of a wave induced by an excitation with a carrier frequency of ∼12.5 kHz, polarized parallel to the DW, which features localization along the edge (of the fragile phase only, consistent with the eigenmode prediction). In summary, in all cases, we record strong localization that persists even deep into the propagation process, before reflections from the opposite boundary begin to interfere with the incident wave to form a standing pattern.

P.A. acknowledges the support of the UMN CSE Graduate Fellowship. S.G. acknowledges support from the National Science Foundation (Grant No. CMMI-2027000). S.S. and K.S. acknowledge the support from the Office of Naval Research (Grant No. MURI N00014-20-1-2479).

[1] J. C. Maxwell, L. On the calculation of the equilibrium and stiffness of frames, London, Edinburgh Dublin Philos. Mag. J. Sci. **27**, 294 (1864).

[2] C. R. Calladine, Buckminster Fuller's tensegrity structures and Clerk Maxwell's rules for the construction of stiff frames, Intl. J. Solids Struct. **14**, 161 (1978).

[3] X. Mao and T. C. Lubensky, Maxwell lattices and topological mechanics, Annu. Rev. Condens. Matter Phys. **9**, 413 (2018).

[4] X. Mao and T. C. Lubensky, Coherent potential approximation of random nearly isostatic kagome lattice, Phys. Rev. E **83**, 011111 (2011).

[5] C. L. Kane and T. C. Lubensky, Topological boundary modes in isostatic lattices, Nat. Phys. **10**, 39 (2014).

[6] T. C. Lubensky, C. L. Kane, X. Mao, A Souslov, and K. Sun, Phonons and elasticity in critically coordinated lattices, Rep. Prog. Phys. **78**, 073901 (2015).

[7] D. Z. Rocklin, S. Zhou, K. Sun, and X. Mao, Transformable topological mechanical metamaterials, Nat. Commun. **8**, 14201 (2017).

[8] L. Zhang and X. Mao, Fracturing of topological Maxwell lattices, New J. Phys. **20**, 063034 (2018).

[9] J. Paulose, A. S. Meussen, and V. Vitelli, Selective buckling via states of self-stress in topological metamaterials, Proc. Natl. Acad. Sci. USA **112**, 7639 (2015).

[10] H. Xiu, H. Liu, A. Poli, G. Wan, K. Sun, E. M. Arruda, X. Mao, and Z. Chen, Topological transformability and reprogrammability of multistable mechanical metamaterials, Proc. Natl. Acad. Sci. USA **119**, e2211725119 (2022).

[11] K. Sun, A. Souslov, X. Mao, and T. C. Lubensky, Surface phonons, elastic response, and conformal invariance in twisted kagome lattices, Proc. Natl. Acad. Sci. USA **109**, 12369 (2012).

[12] H. Danawe, H. Li, H. A. Ba'ba'a, and S. Tol, Existence of corner modes in elastic twisted kagome lattices, Phys. Rev. B **104**, L241107 (2021).

[13] H. Nassar, H. Chen, and G. Huang, Microtwist elasticity: A continuum approach to zero modes and topological polarization in kagome lattices, J. Mech. Phys. Solids **144**, 104107 (2020).

[14] H. Chen, H. Nassar, A. N. Norris, G. K. Hu, and G. L. Huang, Elastic quantum spin Hall effect in kagome lattices, Phys. Rev. B **98**, 094302 (2018).

[15] E. Riva, D. E. Quadrelli, G. Cazzulani, and F. Braghin, Tunable in-plane topologically protected edge waves in continuum kagome lattices, J. Appl. Phys. **124**, 164903 (2018).

[16] M. Schaeffer and M. Ruzzene, Wave propagation in reconfigurable magneto-elastic kagome lattice structures, J. Appl. Phys. **117**, 194903 (2015).

[17] K. Bertoldi, V. Vitelli, J. Christensen, and M. van Hecke, Flexible mechanical metamaterials, Nat. Rev. Mater. **2**, 17066 (2017).

[18] P. Azizi, S. Sarkar, K. Sun, and S. Gonella, Dynamics of self-dual kagome metamaterials and the emergence of fragile topology, Phys. Rev. Lett. **130**, 156101 (2023).

[19] M. Charara, K. Sun, X. Mao, and S. Gonella, Topological flexural modes in polarized bilayer lattices, Phys. Rev. Appl. **16**, 064011 (2021).

[20] C. Widstrand, C. Hu, X. Mao, J. Labuz, and S. Gonella, Stress focusing and damage protection in topological Maxwell metamaterials, Intl. J. Solids Struct. **274**, 112268 (2023).

[21] H. Chen, S. Wang, X. Li, and G. Huang, Two-dimensional microtwist modeling of topological polarization in hinged kagome lattices and its experimental validation, Intl. J. Solids Struct. **254-255**, 111891 (2022).

[22] J. Ma, D. Zhou, K. Sun, X. Mao, and S. Gonella, Edge modes and asymmetric wave transport in topological lattices: Experimental characterization at finite frequencies, Phys. Rev. Lett. **121**, 094301 (2018).

[23] Z.-D. Zhang, M.-H. Lu, and Y.-F. Chen, Twist-angle-induced boundary-obstructed topological insulator on elastic kagome metamaterials, Phys. Rev. Appl. **20**, 054002 (2023).

[24] H. C. Po, H. Watanabe, and A. Vishwanath, Fragile topology and Wannier obstructions, Phys. Rev. Lett. **121**, 126402 (2018).

[25] B. Bradlyn, Z. Wang, J. Cano, and B. A. Bernevig, Disconnected elementary band representations, fragile topology, and wilson loops as topological indices: An example on the triangular lattice, Phys. Rev. B **99**, 045140 (2019).

[26] J. Ahn, S. Park, and B.-J. Yang, Failure of Nielsen-Ninomiya theorem and fragile topology in two-dimensional systems with space-time inversion symmetry: Application to twisted bilayer graphene at magic angle, Phys. Rev. X **9**, 021013 (2019).

[27] A. Bouhon, A. M. Black-Schaffer, and R.-J. Slager, Wilson loop approach to fragile topology of split elementary band representations and topological crystalline insulators with time-reversal symmetry, Phys. Rev. B **100**, 195135 (2019).
[28] B. J. Wieder and B. A. Bernevig, The axion insulator as a pump of fragile topology, arXiv:1810.02373.
[29] Z.-D. Song, L. Elcoro, and B. A. Bernevig, Twisted bulk-boundary correspondence of fragile topology, Science **367**, 794 (2020).
[30] V. Peri, Z.-D. Song, M. Serra-Garcia, P. Engeler, R. Queiroz, X. Huang, W. Deng, Z. Liu, B. A. Bernevig, and S. D. Huber, Experimental characterization of fragile topology in an acoustic metamaterial, Science **367**, 797 (2020).
[31] B. J. Wieder, Z. Wang, J. Cano, X. Dai, L. M. Schoop, B. Bradlyn, and B. A. Bernevig, Strong and fragile topological Dirac semimetals with higher-order Fermi arcs, Nat. Commun. **11**, 627 (2020).
[32] B. Lian, F. Xie, and B. A. Bernevig, Landau level of fragile topology, Phys. Rev. B **102**, 041402(R) (2020).
[33] A. Bouhon, T. Bzdušek, and R.-J. Slager, Geometric approach to fragile topology beyond symmetry indicators, Phys. Rev. B **102**, 115135 (2020).
[34] M. B. de Paz, M. G. Vergniory, D. Bercioux, A. García-Etxarri, and B. Bradlyn, Engineering fragile topology in photonic crystals: Topological quantum chemistry of light, Phys. Rev. Res. **1**, 032005(R) (2019).
[35] V. Peri, Z.-D. Song, B. A. Bernevig, and S. D. Huber, Fragile topology and flat-band superconductivity in the strong-coupling regime, Phys. Rev. Lett. **126**, 027002 (2021).
[36] Y. Xu, M. G. Vergniory, D.-S. Ma, J. L. Mañes, Z.-D. Song, B. A. Bernevig, N. Regnault, and L. Elcoro, Catalogue of topological phonon materials, arXiv:2211.11776.
[37] F. N. Ünal, A. Bouhon, and R.-J. Slager, Topological euler class as a dynamical observable in optical lattices, Phys. Rev. Lett. **125**, 053601 (2020).
[38] B. Peng, A. Bouhon, B. Monserrat, and R.-J. Slager, Phonons as a platform for non-Abelian braiding and its manifestation in layered silicates, Nat. Commun. **13**, 423 (2022).
[39] S. Kooi, G. van Miert, and C. Ortix, The bulk-corner correspondence of time-reversal symmetric insulators, npj Quantum Mater. **6**, 1 (2021).
[40] A. Alexandradinata, J. Höller, C. Wang, H. Cheng, and L. Lu, Crystallographic splitting theorem for band representations and fragile topological photonic crystals, Phys. Rev. B **102**, 115117 (2020).
[41] M. Fruchart, Y. Zhou, and V. Vitelli, Dualities and non-Abelian mechanics, Nature (London) **577**, 636 (2020).
[42] H. Danawe, H. Li, K. Sun, and S. Tol, Finite-frequency topological Maxwell modes in mechanical self-dual kagome lattices, Phys. Rev. Lett. **129**, 204302 (2022).
[43] E. C. Marino, L. O. Nascimento, V. S. Alves, and C. M. Smith, Interaction induced quantum valley Hall effect in graphene, Phys. Rev. X **5**, 011040 (2015).
[44] R. K. Pal and M. Ruzzene, Edge waves in plates with resonators: An elastic analogue of the quantum valley Hall effect, New J. Phys. **19**, 025001 (2017).
[45] J. Ma, K. Sun, and S. Gonella, Valley Hall in-plane edge states as building blocks for elastodynamic logic circuits, Phys. Rev. Appl. **12**, 044015 (2019).
[46] T.-W. Liu and F. Semperlotti, Experimental evidence of robust acoustic valley Hall edge states in a nonresonant topological elastic waveguide, Phys. Rev. Appl. **11**, 014040 (2019).
[47] K. Qian, D. J. Apigo, C. Prodan, Y. Barlas, and E. Prodan, Topology of the valley-Chern effect, Phys. Rev. B **98**, 155138 (2018).
[48] H. Pan, X. Li, F. Zhang, and S. A. Yang, Perfect valley filter in a topological domain wall, Phys. Rev. B **92**, 041404(R) (2015).
[49] Y. Chen, X. Liu, and G. Hu, Topological phase transition in mechanical honeycomb lattice, J. Mech. Phys. Solids **122**, 54 (2019).
[50] X. Wu, Y. Meng, J. Tian, Y. Huang, H. Xiang, D. Han, and W. Wen, Direct observation of valley-polarized topological edge states in designer surface plasmon crystals, Nat. Commun. **8**, 1304 (2017).
[51] See Supplemental Material at http://link.aps.org/supplemental/10.1103/PhysRevB.110.L060102 for details, including the following: design process of deriving two topologically distinct lattices and topological phonon band inversion, $\mathbf{k}\cdot\mathbf{p}$ Hamiltonian and Jackiw-Rebbi analysis of the DW mode, experimental setup, and full-scale steady-state simulation transmissibility curve.
[52] M. I. Aroyo, J. M. Perez-Mato, D. Orobengoa, E. S. Tasci, G. de la Flor Martin, and A. Kirov, Crystallography online: Bilbao crystallographic server, Bulg. Chem. Commun. **43**, 183 (2011).
[53] M. I. Aroyo, J. M. Perez-Mato, C. Capillas, E. Kroumova, S. Ivantchev, G. Madariaga, A. Kirov, and H. Wondratschek, Bilbao crystallographic server: I. Databases and crystallographic computing programs, Z. Kristallogr. Cryst. Mater. **221**, 15 (2006).
[54] M. I. Aroyo, A. Kirov, C. Capillas, J. M. Perez-Mato, and H. Wondratschek, Bilbao crystallographic server. II. Representations of crystallographic point groups and space groups, Acta Crystallogr. Sect. A: Found. Crystallogr. **62**, 115 (2006).
[55] M. G. Vergniory, L. Elcoro, Z. Wang, J. Cano, C. Felser, M. I. Aroyo, B. A. Bernevig, and B. Bradlyn, Graph theory data for topological quantum chemistry, Phys. Rev. E **96**, 023310 (2017).
[56] L. Elcoro, B. Bradlyn, Z. Wang, M. G. Vergniory, J. Cano, C. Felser, B. A. Bernevig, D. Orobengoa, G. de la Flor, and M. I. Aroyo, Double crystallographic groups and their representations on the Bilbao Crystallographic Server, J. Appl. Crystallogr. **50**, 1457 (2017).
[57] B. Bradlyn, L. Elcoro, J. Cano, M. G. Vergniory, Z. Wang, C. Felser, M. I. Aroyo, and B. A. Bernevig, Topological quantum chemistry, Nature (London) **547**, 298 (2017).
[58] J. Cano, B. Bradlyn, Z. Wang, L. Elcoro, M. G. Vergniory, C. Felser, M. I. Aroyo, and B. A. Bernevig, Building blocks of topological quantum chemistry: Elementary band representations, Phys. Rev. B **97**, 035139 (2018).
[59] R. Jackiw and C. Rebbi, Solitons with fermion number, Phys. Rev. D **13**, 3398 (1976).
[60] M. S. Dresselhaus, G. Dresselhaus, and A. Jorio, *Group Theory: Application to the Physics of Condensed Matter* (Springer, Berlin, 2007).